nature energy

Article

https://doi.org/10.1038/s41560-023-01202-1

Growing single-crystalline seeds on lithiophobic substrates to enable fast-charging lithium-metal batteries

Received: 23 September 2022

Accepted: 11 January 2023

Published online: 09 February 2023

Check for updates

Zhaohui Wu[1], Chunyang Wang[2], Zeyu Hui[3], Haodong Liu[3], Shen Wang[3], Sicen Yu[4], Xing Xing[4], John Holoubek[3], Qiushi Miao[4], Huolin L. Xin[2] ✉ & Ping Liu[1,3,4] ✉

Controlling the nucleation and growth of lithium metal is essential for realizing fast-charging batteries. Here we report the growth of single-crystalline seeds that results in the deposition of dense lithium, even at high current densities. Contrary to the widely accepted practice of using a lithiophilic surface to achieve dendrite-free deposition, we employ a lithiophobic surface made of a nanocomposite of LiF and Fe to deposit hexagonal crystals, which induce subsequent dense lithium deposition. The nanocomposites have uniform Fe sites for nucleation while LiF enables rapid lithium transport. A cell using a 3 mAh cm^{-2} $LiNi_{0.8}Co_{0.1}Mn_{0.1}O_2$ (LiNMC811) cathode, onefold excess of lithium and 3 g Ah^{-1} electrolyte cycles at a 1 C rate for more than 130 cycles with 80% capacity retention, a 550% improvement over the baseline cells. Our findings advance the understanding of lithium nucleation and pave the way for realizing high-energy, fast-charging Li-metal batteries.

Lithium-metal batteries (LMBs) are under intensive development due to their promise of high energy densities for applications in electric vehicles and portable electronics[1–16]. It is generally accepted that the stability of the Li-metal anode determines the cycle life of these batteries[17–25]. Controlling the nucleation and growth of Li metal is thus critical. Both chemical and mechanical approaches have been applied. The development of new electrolytes, as represented by the localized high-concentration electrolytes[4,6,7,16,26–28], has advanced the cycle life of LMBs substantially, culminating in a recent demonstration of cell energy densities of 350 Wh kg^{-1} and cycle life of 600 cycles (ref. [6]). With regard to mechanical control, applying a pressure of 1,200 kPa has been shown to effectively reduce Li-metal porosity increase and extend the cycle life of LMBs, although practical implementation of such pressure in commercial-format cells will be challenging[12,15,29].

Despite these performance advancements, the fundamental mechanisms that determine Li nucleation and growth remain a topic of ongoing study. Two factors are of primary importance: the electrolyte and the substrate. High-performance electrolytes usually promote the formation of a LiF-rich solid electrolyte interface (SEI) layer on deposited Li metal[3,10,30–32]. The high surface energy between these two materials ensures rapid diffusion of Li at the Li/SEI interface, which is one of the most critical interfaces in LMBs and essential for non-dendritic growth. In the meantime, as energy-dense LMBs with low negative/positive (N/P) ratio are desired[33] (ideally, anode-free batteries), where lithium must also be deeply plated/stripped, regulation of lithium nucleation and early growth on a foreign substrate also play a major role in improving cyclability. Thus, transport of Li at the Li/substrate interface could be as essential as the transport at the Li/SEI interface, especially for the initial Li nucleation and growth. As a previous study shows[34], with fast Li diffusion on both the Li/SEI interface and Li/substrate interface, the quick 'self re-arrangement' enables the early nucleation, and growth of lithium progresses in a more planar manner.

[1]Program of Chemical Engineering, University of California San Diego, La Jolla, CA, USA. [2]Department of Physics and Astronomy, University of California, Irvine, CA, USA. [3]Department of NanoEngineering, University of California San Diego, La Jolla, CA, USA. [4]Program of Material Science, University of California San Diego, La Jolla, CA, USA. ✉e-mail: huolinx@uci.edu; piliu@ucsd.edu

https://doi.org/10.1038/s41560-023-01202-1

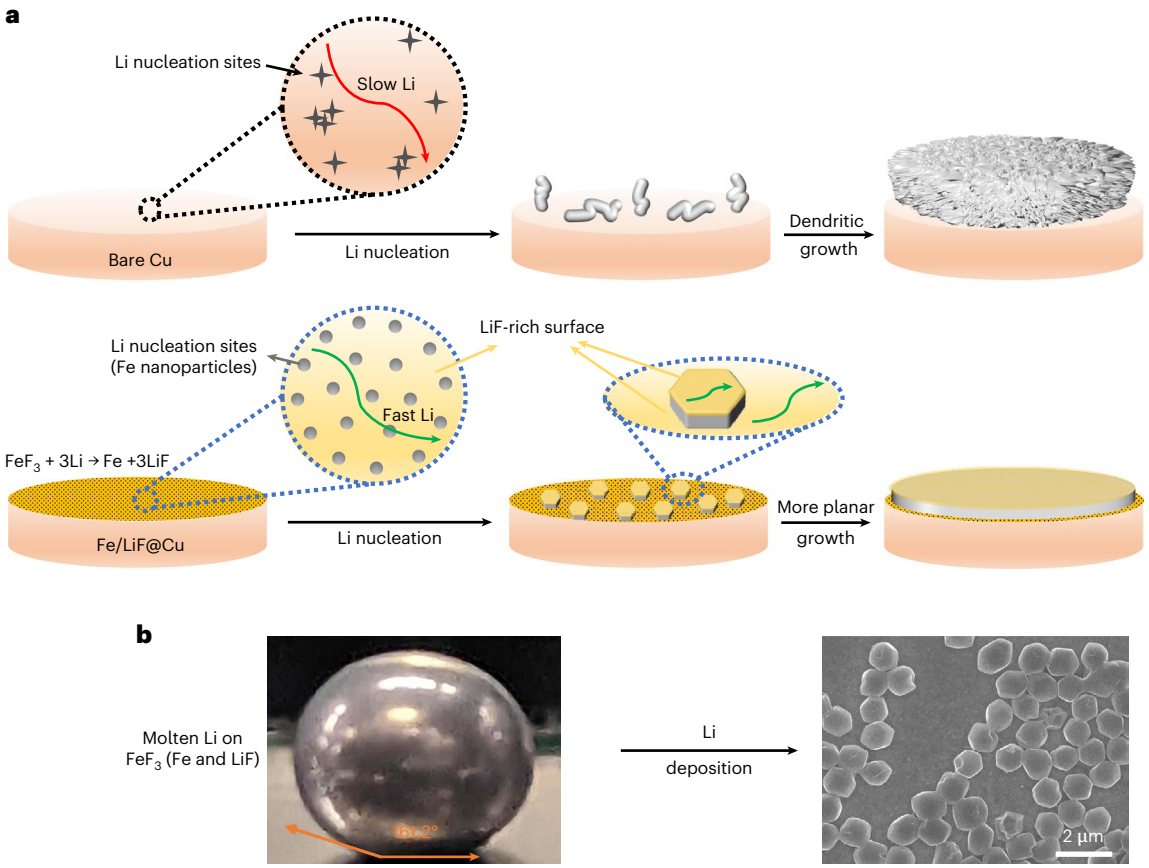

Fig. 1 | Li nucleation and growth on different substrates. a, Schematic illustration of Li plating onto different substrates. Fe/LiF nanocomposite regulates Li nucleation and growth, resulting in a dense Li deposition. **b**, Wetting angle of molten lithium on FeF_3 and SEM image of Li deposition. Tests are conducted at 300 °C. SEM images of 0.1 mAh cm^{-2} Li deposited on Fe/LiF nanocomposite at 3 mA cm^{-2}.

As far as the effect of substrates, lithium deposition is also observed to be facilitated by a high affinity with the substrate material[35–40]. In other words, lithium metal needs to 'wet' the substrate. In fact, the wetting angle of lithium is widely used as a metric to predict the nucleation of lithium. To take the concept one step further, metals (for example, Ag and Au) capable of forming alloys are often used to reduce barriers for lithium deposition[41,42]. Non-dendritic seeds have a semi-spherical shape, which presumably grow into large 'chunks' with smooth edges as the deposition progresses.

One fundamental issue of a sphere-particle-based growth model lies in its limitation in approaching a porosity-free Li electrode. Although applying high pressure has been found to be helpful, ideally, lithium should grow in a planar manner instead of a porous manner to minimize porosity. In crystal growth theory, planar growth requires rapid lateral diffusion of the metal atoms[43]. In the case of Li seeds on a substrate, Li diffusion rates need to be fast at both the Li/SEI and the Li/substrate interfaces. While a LiF-rich SEI has addressed this issue at the Li/SEI interface, the Li/substrate interface remains a challenge. In fact, wetting by Li on a substrate due to a strong affinity does not necessarily promote rapid lateral lithium diffusion. Because Li is known to diffuse fast at a Li/LiF interface, the substrate should also be ideally covered with LiF. However, LiF is a known insulator and cannot be used as a substrate by itself.

The current work overcomes this challenge with a Fe/LiF nanocomposite substrate and demonstrates the growth of single-crystalline Li seeds enabled by this rapid transport mechanism. Such growth persists even at a current density of 5 mA cm^{-2}. These faceted crystalline seeds evolve into a dense Li layer as the deposition continues and virtually eliminate the porosity near the substrate, a phenomenon suffered by a Cu substrate. Leveraging the dendrite-free and dense Li deposition, we demonstrate much-improved cycling stability of $LiNi_{0.8}Co_{0.1}Mn_{0.1}O_2$ (Li/NMC811) full cells at a 1 C rate. Our results invite more in-depth examination of the mechanisms for nucleation and growth of lithium metal, essential for realizing batteries capable of fast charging and discharging.

Li nucleation behaviour

To enable Li growth between two LiF-rich surfaces that promote rapid lateral lithium diffusion, we designed a Fe/LiF nanocomposite-modified Cu substrate for lithium deposition. A thin film of FeF_3 is converted in situ to generate a uniform Fe/LiF nanocomposite (Fig. 1a). Our previous study has shown that the lithiation of iron halogen compounds generate ~2 nm metal particles, much smaller than copper and other transition metals[44]. We hypothesize that the nanosized Fe particles provide abundant and uniformly distributed nucleation sites for Li, leading to a uniform Li seeding at the initial deposition stage, while the LiF promotes rapid lithium diffusion[20,45,46]. As shown in Fig. 1a, the regulated nucleation and initial growth on the Fe/LiF nanocomposite results in a denser Li layer in the subsequent deposition. In contrast, the dendritic initial growth on Cu leads to a highly porous Li deposit. The full-cell cyclability will be greatly affected by the Li structure because the pores consume a large amount of electrolyte. Regulating the initial stage of Li growth is essential to mitigate porosity growth and cell failure due to electrolyte dry out.

The FeF_3 substrate is prepared by thermal evaporation of FeF_3 powder onto Cu. Top-view scanning electron microscopy (SEM) image of the obtained film shows a crack-free morphology (Supplementary Fig. 1a). The thickness of the film is ~270 nm as determined

https://doi.org/10.1038/s41560-023-01202-1

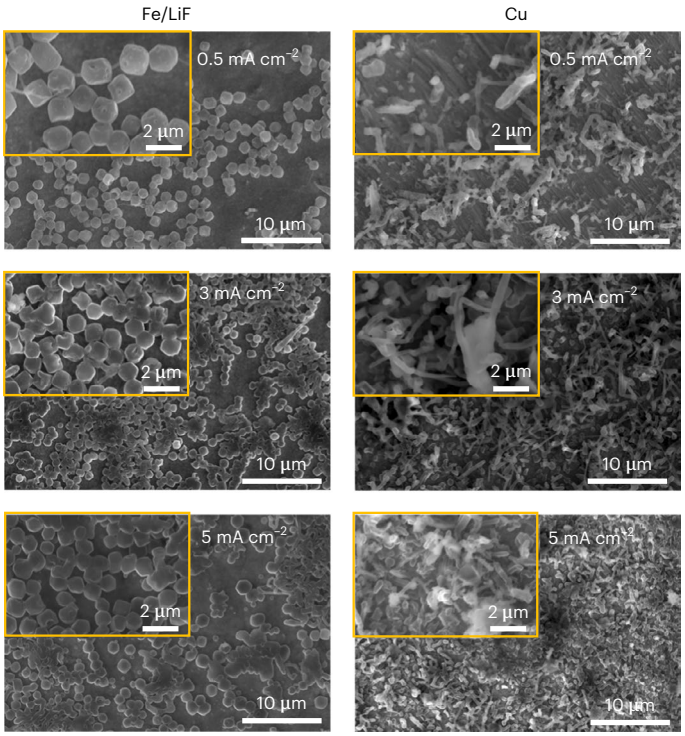

Fig. 2 | Morphology of initial Li deposition on different substrates. SEM images of 0.1 mAh cm^{-2} Li deposited on the Fe/LiF nanocomposite or Cu substrate, under different current densities, including 0.5, 3 and 5 mA cm^{-2}. Insets: higher-magnification images.

from the cross-sectional-view image obtained by focused ion beam scanning electron microscopy (FIB-SEM) (Supplementary Fig. 1b). Energy-dispersive X-ray spectroscopy of the FeF_3 thin film shows a uniform Fe and F distribution (Supplementary Fig. 1c,d). The FeF_3 thin film prepared by thermal evaporation appears to be amorphous as shown by Supplementary Fig. 2. The amorphous nature of thermal evaporated FeF_3 has been previously reported by literature[47]. Despite the absence of crystallinity, X-ray photoelectron spectroscopy (XPS) data (Supplementary Fig. 3) are collected to estimate the chemical composition of the thin film. The elemental ratio between Fe and F is 1:3. (Supplementary Table 1). Therefore, the obtained sample is a 200–300 nm-thick uniform FeF_3 thin film.

We first evaluate the wetting of Li on the FeF_3 substrate. As has been previously shown where FeF_3 was studied as a cathode-active material, when FeF_3 is lithiated (discharged) to below 1 V, the FeF_3 will fully convert into Fe and LiF (more details are provided below by transmission electron microscopy (TEM) analysis)[48]. As expected, Li has a contact angle of 161.2° (Fig. 1b), much higher than Li on Fe substrate (106.5°), even higher than 137.1° measured on a Ti substrate (Supplementary Fig. 4) and the values reported for Cu, Ni and other similar metals[49].

To investigate how the substrate affects the nucleation and initial growth of Li, 0.1 mAh cm^{-2} Li is deposited on Fe/LiF nanocomposite and Cu, after first discharging to 0 V. The electrolyte, 2 M lithium bis(fluorosulfonyl)imide (LiFSI) in 1,2-dimethoxyethane/bis(2,2,2-trifluoroethyl) ether (DME/BTFE) (1:4 by weight) (LDME), is a state-of-art electrolyte offering high Li efficiency (>99%) and dendrite-free Li morphology[7]. The SEM images of Li deposition are shown in Fig. 2 and Supplementary Fig. 5. Despite the fact that Li deposition in LDME electrolyte is often shown to be dendrite free, to our surprise, the initial Li growth on Cu shows randomly oriented dendritic morphology. This is likely a result of the non-uniform and chemical nature of the Cu substrate. With low surface Li diffusivity and lacking nucleation sites, lithium would preferably deposit locally at selected sites with low nucleation energy (for example, high-energy grain-boundary sites). As a result, the actual local current density is very high, which would promote a dendritic morphology. We note that such 'patchy' behaviour of deposition on Cu in the initial stage is widely reported[8,28,33,50]. Furthermore, the inhomogeneous nucleation site phenomenon is not limited to Cu. In fact, even when depositing Li on a Li foil, non-uniform and even dendrite morphology have also been observed (Supplementary Fig. 6).

In contrast, the images of 0.1 mAh cm^{-2} Li deposited on Fe/LiF nanocomposite reveal uniformly distributed micron-size hexagonal crystals. The hexagonal crystals grown on the Fe/LiF substrate represent near thermodynamically equilibrated growth owing to highly uniform nucleation sites and facilitated lithium transport at both the lithium/substrate interface and the lithium/SEI interface due to the presence of LiF. As a previous report has shown, a triagonal or hexagonal cross section is appropriate for Li, a body-centred cubic (bcc) crystal, to expose {110} low-energy planes at all three or six facets[51]. Furthermore, we have found that the hexagonal crystal feature persists up to 5 mA cm^{-2}, indicating the fast-charging capability of Li anode using the Fe/LiF nanocomposite-modified Cu (Fig. 2 and Supplementary Fig. 5). We note that the Li crystals are not perfectly aligned in crystal orientation although they have similar sizes. The optical images of the deposited Li show the morphological difference at a macroscopic scale (Supplementary Fig. 7). The Li deposited on Fe/LiF nanocomposite shows a silver colour, while the one on Cu is darker, which is typically associated with an irregular morphology. This macroscopic difference is related to the uniformity of nucleation site distribution. Fe sites are generated in situ and are inherently uniformly distributed with near identical size and structures. As a result, lithium nucleation can take place on all of them simultaneously. This uniformity itself is insufficient to generate single-crystalline seeds, however. When Fe_2O_3 is evaporated on Cu and used as substrate for Li deposition, Li grows as dendrites (Supplementary Fig. 8), clearly indicating that due to high surface Li diffusion, LiF-rich substrate facilitates the growth of deposited lithium towards its thermodynamically stable morphology. Additionally, to probe the importance of Cu current collector underneath the Fe/LiF coating, we evaporated FeF_3 on Ti foil. The initial Li deposition still manifests in a hexagonal single-crystal morphology (Supplementary Fig. 9).

Our results thus show that to grow dense lithium with low porosity, the substrate is not necessarily lithiophilic, although lithiophobicity is unlikely to be required either. What matters is rapid Li transport at the Li/substrate interface. As will be shown later, fast Li transport on Li/substrate interface enables faceted lithium nucleation and growth, leading to low-porosity Li deposition, which persists even after high-capacity deposition.

TEM observation of single-crystalline Li seeds

We next perform cryogenic TEM characterization of the Fe/LiF nanocomposite substrate and the deposited Li crystals in their native states (Methods). Figure 3a–c shows the image and diffraction patterns of the FeF_3 thin film after electrochemical Li deposition. Dark-field cryoEM image, as shown in Fig. 3a (large field-of-view image in Supplementary Fig. 10), is formed by selecting part of the scattered electrons with an objective aperture (the direct electron beam is unselected). The areas where the electron scattering is selected will be brighter, while the areas with electron scattering not selected will appear dark. The bright features (indicated by arrows) in the dark-field TEM image indicate that nanosized domains are formed, which is verified by atomic-resolution imaging showing the formation of bcc Fe nanoparticles with a size of ~2 nm and the presence of disordered/amorphous domains (Fig. 3b). Considering the clear existence of LiF observed in the F 1*s* XPS spectra (Supplementary Fig. 11) and given the disordered nature of LiF from FeF_3 lithiation reported previously[52], we conclude that the amorphous domain is LiF. The electron-diffraction pattern shows that the reacted

https://doi.org/10.1038/s41560-023-01202-1

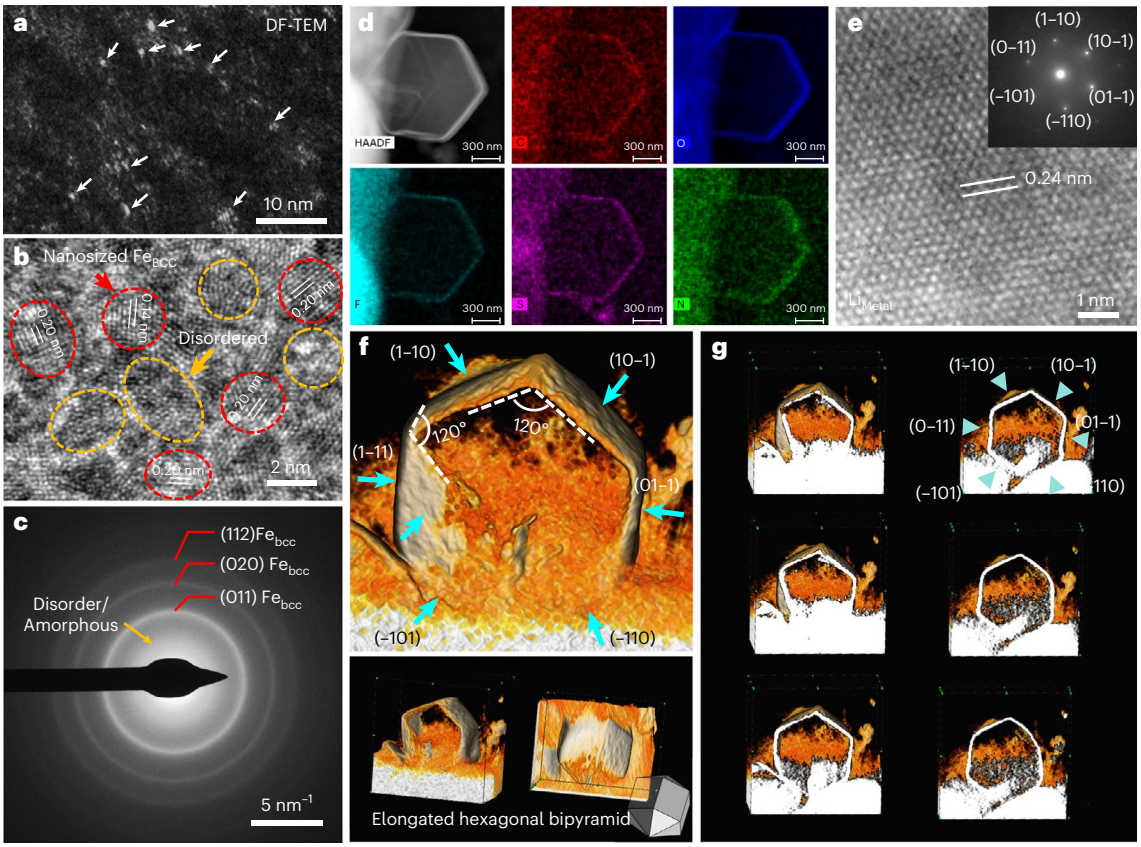

Fig. 3 | Cryo-TEM imaging and crystallographic analysis of the single-crystalline Li crystals. a, Dark-field TEM (DF-TEM) image showing the formation of nanosized domains (examples indicated by arrows) in the substrate after electrochemical Li deposition. **b**, Atomic-resolution TEM image showing the formation of sub-nano (<10 nm) bcc Fe nanoparticles (red circles) and disordered/amorphous domains (orange circles). The measured lattice spacing of 0.20 nm and 0.14 nm can be assigned to the (110) and (200) planes of bcc Fe, respectively. **c**, Electron-diffraction pattern of the reacted substrate showing diffraction rings corresponding to bcc Fe and halo pattern corresponding to amorphous phase. **d**, EDS maps of C, O, F, S, N. The result shows that a thin layer of uniform SEI forms on the surface of the Li crystal. HAADF, high-angle angular dark field. **e**, Atomic-resolution TEM image of the Li metal obtained along the [111] zone axis. The electron-diffraction pattern in the inset shows that the Li crystal in **d** is perfectly single-crystalline. **f**, Three-dimensional imaging of the hexagonal-shaped single-crystalline Li metal in **d** by cryo-TEM tomography. The single-crystalline Li metal has a near-elongated hexagonal bipyramidal shape mainly terminated with low-energy {110} facets. **g**, The cross-section analysis highlights the elongated prism-side surfaces corresponding to the {110} planes of bcc Li metal.

Fe/LiF nanocomposite substrate has Bragg rings corresponding to bcc Fe. The halo pattern probably corresponds to the disordered or amorphous LiF.

Figure 3d–f shows the cryo imaging of the plated Li crystal. The energy-dispersive X-ray spectroscopic (EDS) images in Fig. 3d show the deposited Li crystal has a thin, conformal SEI film that contains C, O, F, S and N, which could be a gradient layer derived from the lithiation of fluoride, according to a previous report[40], while the high-intensity signal of F on the substrate is dominated by the contribution from the LiF/Fe film. Figure 3e and the inset shows that the hexagonally shaped Li crystal indeed is a single crystal—both the high-resolution cryo-TEM image and the diffraction pattern show a perfect hexagonal symmetry down the [111] zone axis. We further perform cryo-electron tomography to image the three-dimensional (3D) shape of the Li crystal. The 3D reconstruction in Fig. 3f shows the single-crystalline Li metal has a near-elongated hexagonal bipyramidal shape mainly terminated with low-energy {110} facets. Previous theoretical models indicate that [100] is the most stable facet for Li metal[53–55]. However, [110] facet has been observed in electrodeposited Li metals[56]. The hexagonal shape we have observed thus represents the Wulff shape of Li metal.

The evolution of Li morphology during subsequent growth

We then examine the effect of single-crystalline Li-metal seeds on the subsequent growth of Li-metal layers to reach a capacity that is relevant to a practical battery. Although the crystalline seeds are not perfectly aligned in their orientation (Fig. 2a), they still provide notable benefit in growth of low-porosity Li. To study whether the Li regulation effect still persists when the layer grows thicker, we gradually increased the deposition capacity from 0.1 mAh cm^{-2} to 3 mAh cm^{-2}. The top-view SEM images are shown in Supplementary Fig. 12. As the capacity increases, the hexagonal Li crystals gradually merge to form a substrate with uniform Li orientation. Meanwhile, another layer of Li starts to be plated on top of the smooth Li substrate, which appears to be dendrite free and dense. The uniform Li deposition continues as capacity increases from 0.5 mAh cm^{-2} to 3 mAh cm^{-2}. On the contrary, Li deposited on Cu starts with randomly oriented Li filaments. As deposition capacity increases from 0.1 mAh cm^{-2} to 1 mAh cm^{-2}, the filaments grow thicker but do not vanish. Only when 3 mAh cm^{-2} is deposited, the Li merges into granular deposits. The different Li morphology evolution behaviour indicates that the substrate effect remains as the deposition continues.

To understand the effect of current density, 1 mAh cm^{-2} Li is deposited under different current densities, ranging from 0.5 mAh cm^{-2} to 5 mA cm^{-2}. Figure 4a and Supplementary Fig. 13 show the cross-sectional SEM images of the deposited Li, where substantial thickness differences are observed between the Fe/LiF nanocomposite and Cu sample, especially at high current densities. The thicknesses of Li layers on Fe/LiF nanocomposite at 0.5, 1, 3 and 5 mA cm^{-2}, are 6.1, 6.7, 7.3 and 8.7 µm, while the ones on Cu are 8.5, 10.1 15.8 and 17.8 µm, respectively. The theoretical thickness of 1 mAh cm^{-2} Li is 4.85 µm at 0% porosity.

https://doi.org/10.1038/s41560-023-01202-1

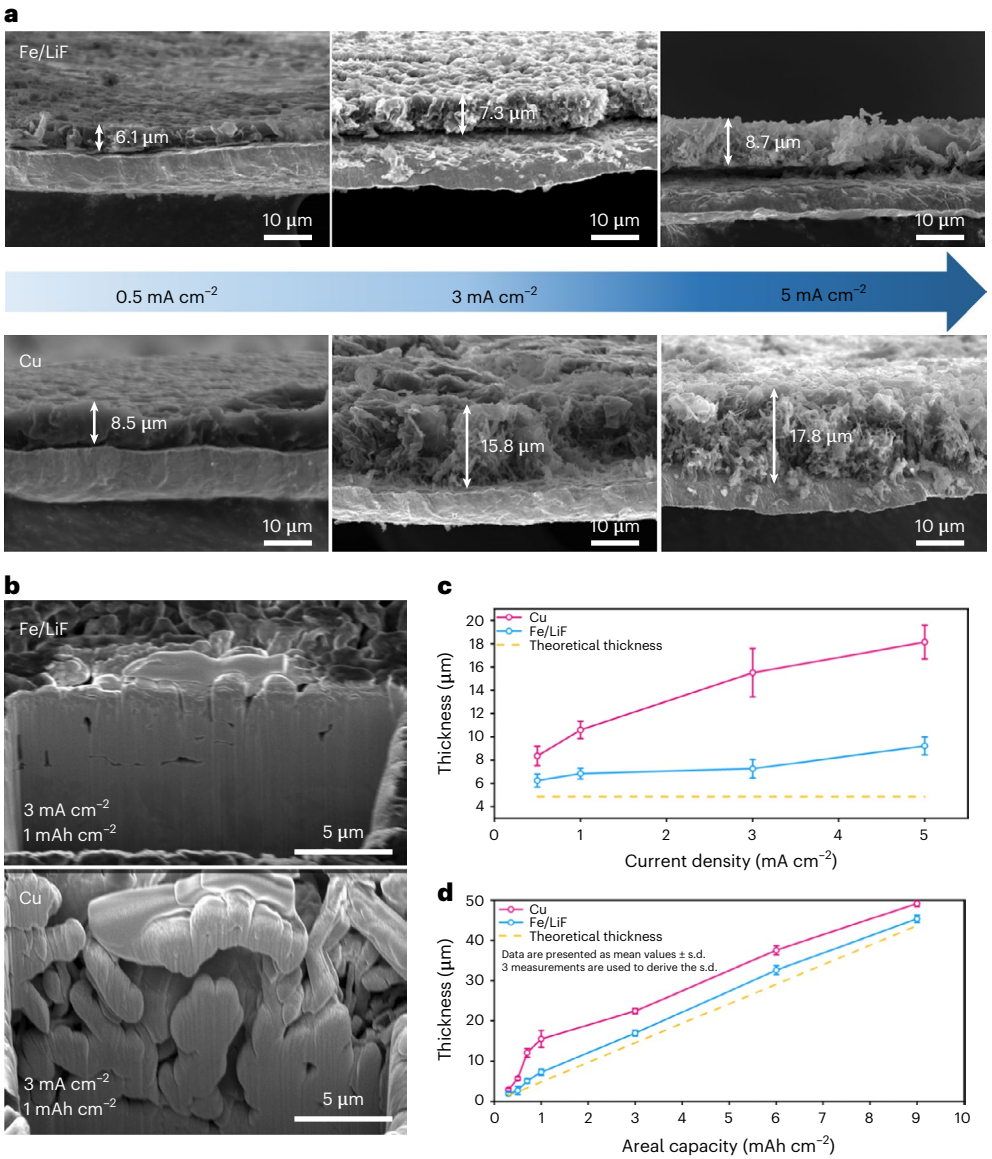

Fig. 4 | Cross-sectional morphology and thickness of the deposited Li layer. **a**, SEM images of 1 mAh cm^{-2} Li plated on the Fe/LiF nanocomposite and Cu substrate, under 0.5, 3, 5 mA cm^{-2}. **b**, Cryo-FIB-SEM images of 1 mAh cm^{-2} Li deposited on the Fe/LiF nanocomposite and Cu substrate under 3 mA cm^{-2}. **c**, Summarized average thickness data (± s.d.) of 1 mAh cm^{-2} Li deposited on Fe/LiF nanocomposite and Cu substrate under different current. **d**, Summarized average thickness data (± s.d.) of different amounts of Li deposited on Fe/LiF nanocomposite and Cu substrate under 3 mA cm^{-2}. The error bars in **c**,**d** are the standard deviation of the Li-layer thickness measured from three SEM images. The SEM images corresponding to the error bars are shown in Supplementary Figs. 14–17.

The fact that Li layers deposited on Cu, especially at high current densities, are more than three times thicker than the fully dense Li indicates their high porosity. Cryo-FIB-SEM is utilized to examine the Li plated at 3 mA cm^{-2} on different substrates to better reveal the porosity difference. As shown in Fig. 4b, Li deposited on Fe/LiF nanocomposite shows a columnar structure with few sub-micron pores distributed in the Li layer. On the contrary, a few µm-size interconnected pores are observed in Li plated on Cu. The FIB-SEM images thus clearly illustrate how Li is packed differently on different substrates. How the deposition capacity affects the porosity is illustrated in Supplementary Figs. 14 and 15, where the current density is maintained at 3 mA cm^{-2}, but the capacity is varied from 0.3 to 9 mAh cm^{-2}. The Li plated on Fe/LiF nanocomposite is found to be denser than the Cu counterpart, independent of the deposition amount. To better visualize the porosity difference and evolution as current or capacity increases, in Fig. 4c,d, we summarize the thickness data of the Li layer deposited under different current densities (0.5 to 5 mA cm^{-2}, at same capacity, 1 mAh cm^{-2}) and capacity (0.3 to 9 mAh cm^{-2}, at the same current density, 3 mA cm^{-2}). The yellow coloured dashed lines represent the thickness of fully dense Li deposits. The data clearly show that no matter what current or capacity is, the Li plated on Fe/LiF nanocomposite is always much denser than that on Cu. The majority of the improvement, however, is found to be associated with the first 1 mAh cm^{-2} capacity. We believe this is due to the reduction in porosity of dendritic lithium upon further Li deposition with the presence of pressure, as has been observed by previous studies[19,29]. We note that at 9 mAh cm^{-2}, the Li thickness is 45.4 µm, nearly identical to the expected thickness of a fully dense layer. The SEM images we use to obtain the thickness information are included in Supplementary Figs. 14–17. In addition to side-view observations, we also investigated the top-view morphology. SEM images of 1 mAh cm^{-2} Li deposited in 0.5, 1, 3, 5 mA cm^{-2} are shown in Supplementary Fig. 18. It is quite clear that the Li plated on Cu shows more dendritic morphology than the

https://doi.org/10.1038/s41560-023-01202-1

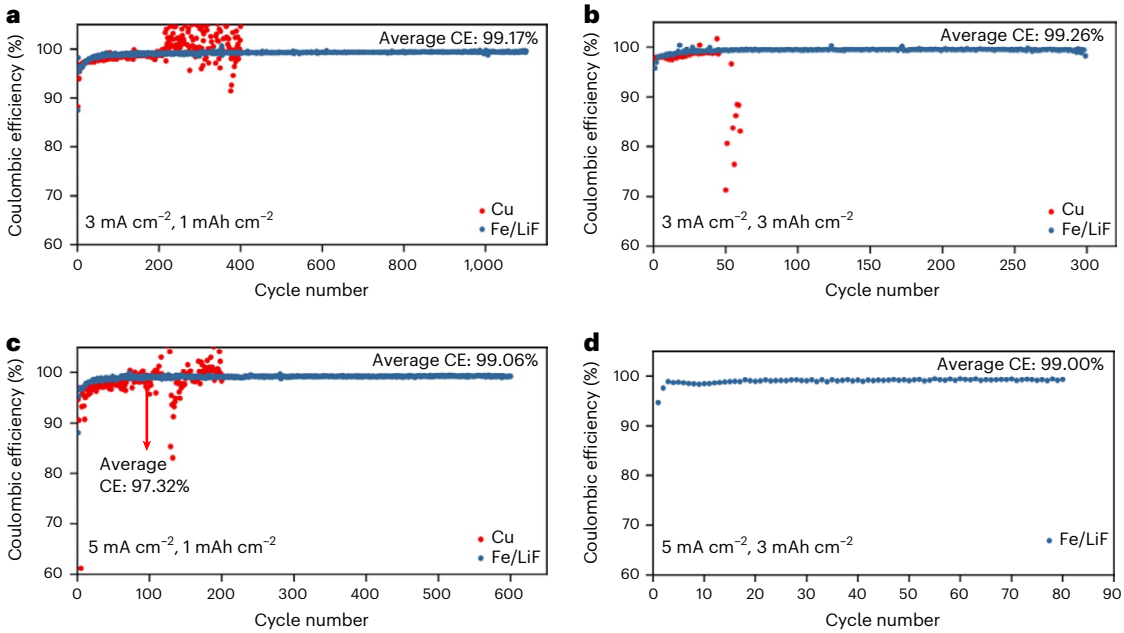

Fig. 5 | Electrochemical performance of half cells with different substrates. a–d, CE versus cycle number of Li||Cu or Fe/LiF nanocomposite cell under different conditions: 3 mA cm^{-2}, 1 mAh cm^{-2} (**a**); 3 mA cm^{-2}, 3 mAh cm^{-2} (**b**); 5 mA cm^{-2}, 1 mAh cm^{-2} (**c**); 5 mA cm^{-2}, 3 mAh cm^{-2} (**d**).

Fe/LiF nanocomposite, especially under high current density, which agrees with our cross-sectional observations.

By investigating the Li morphology evolution at different capacity and current density, we have shown that although high-capacity deposition of Li onto Cu shows reduced porosity due to the presence of pressure[29], the porosity near the substrate from Li nucleation and early growth stage remains. In contrast, the employment of Fe/LiF substrate greatly reduces the initial porosity of Li deposition because the hexagonal Li single crystal formed in the initial Li deposition, even with less than perfect orientation, allows for a much more planar and denser packing of Li, thus promoting low-porosity growth of lithium upon further deposition. We believe such low-porosity plating morphology also helps with uniform stripping of lithium to avoid void formation. Finally, we note that the test conditions we have employed in this study do not trigger a solution transport-limited regime that is characterized by the Sand's capacity (Supplementary Fig. 19).

Half-cell and full-cell battery performance

So far, we have shown that the Fe/LiF nanocomposite substantially influences the Li nucleation behaviour and the initial deposition of single-crystalline Li leads to much-improved morphology and reduced porosity in the following deposition. In principle, better morphology would result in superior cycling performance. Li||Cu or Li||Fe/LiF nanocomposite half cells are constructed to compare their cyclability. Figure 5 shows the Coulombic efficiency (CE) data of half cells tested under different conditions. The corresponding voltage profiles are shown in Supplementary Fig. 20. Current densities of 3 mA cm^{-2} and 5 mA cm^{-2} are used to cycle the batteries because of the remarkable morphological differences observed between the Fe/LiF nanocomposite and Cu samples under such conditions. Lower current-density cycling data are included in Supplementary Fig. 21. In addition to the current-density variation, the cycling capacity is also alternated between 1 mAh cm^{-2} and 3 mAh cm^{-2} to demonstrate the applicability of Fe/LiF nanocomposite in different conditions. Figure 5a,b shows the cycling performance of cells tested under 3 mA cm^{-2} current and 1 mAh cm^{-2} or 3 mAh cm^{-2} capacity, respectively. Remarkably long cycle life of the Fe/LiF nanocomposite cell is observed (>1,000 and 300 cycles, respectively), while the Cu cells shorted quite early due to the high current density. The Cu cell performance deteriorates substantially when the current increases to 5 mA cm^{-2}. The Cu cell shorted at the 113th and 2nd cycles when 1 mAh cm^{-2} and 3 mAh cm^{-2} Li is cycled, respectively, while the Fe/LiF nanocomposite cell delivers 600 and 80 stable cycles under such challenging conditions. The lower voltage on the deposition curve of Fe/LiF near end of plating at high cycle numbers probably indicates a build-up of porosity over the cycling on the counter electrode. We also notice that the average CE of the Cu cell is only 97.32% when 1 mAh cm^{-2} Li is cycled at 5 mA cm^{-2}. In contrast, regardless of cycling conditions, the average CE for the Fe/LiF nanocomposite cell is always >99%. The superior cycling performance and CE of the Fe/LiF nanocomposite cell suggest its promise of application in full cells when cycled at high rates. In addition to the deposition-full-stripping CE measurement, we also apply a partial-stripping measurement following the method proposed by Adam et al.[57]. As shown in Supplementary Fig. 22, a formation cycle of 5 mAh cm^{-2} is performed at 3 mA cm^{-2}. Then another 5 mAh cm^{-2} Li is deposited, which is followed by 1 mAh cm^{-2} ten deposition-stripping cycles at 3 mA cm^{-2}. Finally, the remaining Li is fully stripped. The CE is estimated by comparing the amount stripped after cycling and the amount originally deposited. The Fe/LiF nanocomposite substrate shows a 98.2% CE at such a high current, while the Cu cell shows a 92.9% CE. More importantly, we find that if the formation cycle is performed at 0.5 mA cm^{-2}, there is no CE difference between two different substrates (Supplementary Fig. 22b). Both cells show a 98.9% CE. SEM images (Fig. 2) have shown that even at high current density, the Fe/LiF substrate still manages to provide uniform Li seeding. We believe that the regulated Li seeds formed in the condition cycle leads to the dramatic CE difference. However, if lower current is used in the formation cycle, the uniformity difference in Li seeding is smaller, which results in no CE improvement in the following cycle. This experiment further proves the importance of the substrate and Li nucleation on LMB performance at high current densities.

We then investigate the performance of Fe/LiF nanocomposite substrate in a full cell, which comprises an NMC811 cathode with 3.25 mAh cm^{-2} areal capacity and an anode of either bare Cu or Fe/LiF nanocomposite film with pre-deposited Li. Previous reports have demonstrated that a low N/P (negative/positive, 2–4) ratio and lean-electrolyte (3 g Ah^{-1}) conditions are needed to deliver a

https://doi.org/10.1038/s41560-023-01202-1

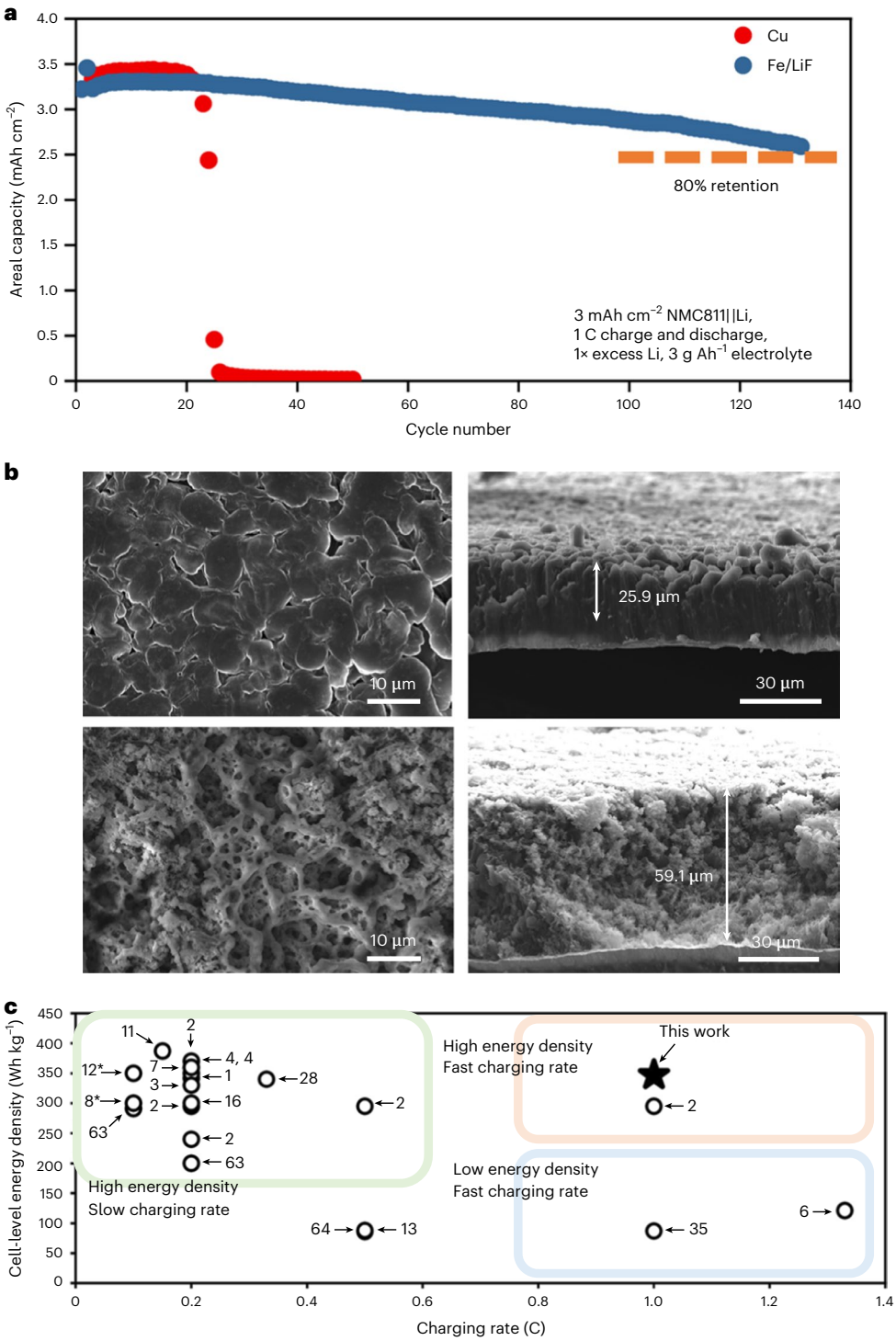

Fig. 6 | Electrochemical performance of full cell with different substrates. **a**, Capacity retention of full cell with 3 mAh cm^{-2} NMC811 as the cathode and 3 mAh cm^{-2} Li plated on different substrates as the anode. The electrolyte (3 g Ah^{-1}) is added to each cell. Constant current constant voltage (CCCV) cycling is performed at 1 C rate, with the voltage window of 2.8–4.4 V. Top view of Fe/LiF (top left) and Cu (bottom left) and cross-sectional view of Fe/LiF (top right) and Cu (bottom left) SEM images of Li morphology after 20 cycles. **c**, Summary of full-cell energy density (by projection, Methods; asterisks indicate measured values) versus charging rate reported in literature[1,2,5–7,10–12,14–16,28,35,63,64].

competitive cell-level energy density (350 Wh kg^{-1}) (refs. [33,39]). In addition to the energy-density consideration, a recent report suggests that a 1:1 N/P ratio helps to prolong cycle life by lowering side reaction rate. Therefore, we deposit 3 mAh cm^{-2} Li on Fe/LiF nanocomposite and Cu, which translates to an N/P ratio of 0.92. The amount of electrolyte added is 3 g Ah^{-1} (only ~10 µl per coin cell). The projected energy density of a 2 Ah pouch cell with aforementioned conditions (areal capacity, electrolyte amount and N/P ratio) is 354.1 Wh kg^{-1}. Detailed calculation is included in Methods. The Li loss due to FeF_3 lithiation is calculated to be 0.074 mAh cm^{-2}, which is negligible compared with deposited Li capacity (3 mAh cm^{-2}). Moreover, in literature reports about Li-anode substrate modification, it is not uncommon that a small fraction of Li inventory is sacrificed to ensure better Li morphology and reversibility[35,38,41,42,58]. In addition to the above-mentioned challenging

condition, NMC811 full cells are cycled at 1 C rate, which corresponds to a current density of 3 mA cm^{-2}. Figure 6a shows the cycling performance comparison of the full cells. The Cu cell lasts only 20 cycles before rapid degradation. The cell capacity decays from >3 mAh cm^{-2} to almost 0 within a few cycles. The degradation symptom is similar to those lean-electrolyte cells reported in the literature, which can be attributed to electrolyte depletion[16,28,39]. It is worth noting that such a phenomenon is typically observed in LMBs with carbonate electrolytes while not in the Li-friendly ether-electrolyte system, largely due to the higher reactivity of the carbonates. However, in our tests, the high current-density deposition poses a great challenge to the Li anode even with electrolytes offering one of the highest CEs, which results in the rapid degradation. On the contrary, the Fe/LiF nanocomposite cell shows stable cycling for 130 cycles before it decays to 80% of its original capacity. Assuming negligible degradation of the cathode capacity, this capacity retention corresponds to a Li cycling efficiency of 99.3%, based on 1× excess Li, much higher than the value obtained in half-cell tests (98.9%). The higher efficiency observed in full cells is due to the inclusion of a constant-voltage step during charging and the effect of the counter electrode as shown previously[59].

To understand the origin of the notably different cyclability, cells are disassembled after 20 cycles to observe the Li morphology. Figure 6b shows top-view and cross-sectional-view SEM images, revealing dramatically different morphology. The Li on the Fe/LiF nanocomposite substrate comprises few-micron-sized Li 'chunks', while that on Cu shows an extremely porous and mossy morphology (Fig. 6b). The cross-sectional images also reveal great differences in Li layer thickness. (Fig. 6b) The Li layer on Fe/LiF nanocomposite is 25.9 µm, while the Li layer on Cu is 59.1 µm. The difference indicates that the substrate effect persists even after repeated cycling. The voltage profile, as shown in Supplementary Fig. 23, also indicates that with the presence of Fe/LiF, the Li-anode impedance evolves much more slowly.

The deposited Li on the Fe/LiF substrate displays substantially reduced porosity compared with Li plated on Cu substrate (Fig. 4d). Such lithium growth originates from the very beginning of deposition as faceted crystals, which ensures uniform current distribution and reductions in electrolyte consumption during subsequent lithium plating and stripping. We believe this low-porosity, more planar lithium morphology, which persists even after high-capacity deposition is responsible for the improved full-cell cycling stability.

In addition to the high-areal-loading full cell, NMC811 cathode with 1.5 mAh cm^{-2} areal loading is also tested under similar conditions, with 1× excess Li and 1 C rate. As shown in Supplementary Figs. 24 and 25, similar improvement is observed.

The above results demonstrate that when combined with lean-electrolyte and fast-charging conditions, the Li regulation effects from Fe/LiF nanocomposite substrate results in notably improved cyclability. To put our results in the context of recently published work, we summarize the reported full-cell cycling data with a controlled amount of excessive Li and electrolyte. The cell-level energy density (by projection or measurement) is plotted against the charging rate in Fig. 6c. Most of the reported data fall into the category of high energy density but low charging rate out of concern for dendrite growth and performance degradation. To enable fast-charging LMB, flooded electrolyte and high N/P ratio are often employed as shown by the light blue line-circled region in Fig. 6c, which decrease the cell-level energy density substantially. On the contrary, our strategy has demonstrated high energy density and fast charging at the same time as highlighted in Fig. 6c.

Conclusion

In summary, we have demonstrated that creating a LiF-rich substrate with nanosized Fe nucleation sites coupled with a high-performance electrolyte promotes the nucleation of Li single-crystal seeds, in contrast to initial dendritic growth on bare Cu. Such regulated Li nucleation and early growth behaviour is enabled by the fast-surface Li diffusion at both the Li/substrate interface and the Li/SEI interface, which are rich in LiF. Our finding shows that the interfacial Li transport rate rather than lithiophilicity determines the Li growth behaviour. With uniform nucleation sites and the low-porosity nature of hexagonal single-crystal Li growth, the commonly observed dendritic growth near the substrate is greatly mitigated.

Leveraging the dendrite-free Li deposition, half cells constructed with Fe/LiF nanocomposite show >1,000 and >600 cycles under 3 and 5 mA cm^{-2}, respectively. Compared with the bare Cu anode substrate, remarkable cyclability improvement is observed in full-cell tests with lean-electrolyte (3 g Ah^{-1}) and 1 C rate cycling, which results from the denser Li deposition. This work presents an approach to tune the Li nucleation behaviour and its consequent Li deposition, which paves the way towards high-energy-density LMBs capable of fast charging, crucial for enabling their application in electric vehicles.

Methods

FeF_3 thin film

The FeF_3 thin film was prepared by thermal evaporation (Angstrom Engineering Nexdep EB Evaporator) of FeF_3 powder (Sigma-Aldrich) at 18% power for 15 mins. Fe_2O_3 thin film was prepared with the same method, but at 28% power for 15 mins.

Cathode

NMC811 was purchased from Targray. A cathode slurry was prepared by mixing NMC811, SuperP and polyvinylidene fluoride in *N*-methylpyrrolidone solution by Thinky mixer. The ratio between the three components is 90:5:5. The slurry was coated on Al foil using a doctor blade. The areal mass loading was controlled at 16 mg cm^{-2} and 8 mg cm^{-2}, respectively. After drying in the vacuum oven at 120 °C overnight, the electrodes were calendared into 30% porosity and then punched into a 12-mm-diameter disk for a coin-cell test.

Electrolyte

Dimethoxyethane was purchased from Gotion. Lithium bis(fluorosulfonyl)imide (LiFSI) was purchased from Sigma-Aldrich. Bis(2,2,2-trifluoroethyl)ether (BTFE) was purchased from Synquest Lab. The LDME electrolyte was prepared by dissolving 2 M LiFSI in DME/BTFE. Here 1 M is defined as 1 M salt dissolved into 1 kg of solvent.

Lithium wetting angle test

Lithium was melted with a hot plate inside an argon-filled glovebox, with O_2 and H_2O levels <0.1 ppm. The molten lithium was cleaned with Ti strip multiple times to remove the reaction products on its surface. For the Li wetting test against FeF_3, FeF_3 was coated on Ti foil at the same thickness as the FeF_3 coated on Cu in electrochemical tests.

Battery assembly

Although pouch cells will offer better pressure control, coin cells have been shown to be a facile platform for Li morphology studies[60–62]; 2016-type and 2032-type coin cells were used for our study.

The 2016-type coin cells were used for Li deposition and half-cell tests. Each cell included a 250 µm Li chip, a 25 µm celgard separator, a 1 mm spacer, a piece of bare Cu or FeF_3 coated Cu and 75 µl electrolyte.

The 2032-type coin cells with Al-coated positive case were used for full-cell tests. The Al-coated case was used to prevent corrosion. A predetermined amount of Li was deposited on Cu or Fe/LiF nanocomposite-modified Cu. Full cells were assembled with NMC811 cathodes, Cu or Fe/LiF nanocomposite-modified Cu with pre-deposited Li, Celgard separators, spacers and springs. The electrolyte amount was controlled as 3 g Ah^{-1}.

Electrochemical testing

Li deposition and half-cell tests were conducted on an LBT-5V5A battery tester (Arbin Instruments). Cells were first discharged at 10 µA until

0.2 V. An additional 24 hour 0.2 V constant voltage hold was applied in the FeF_3 cells to fully lithiate the thin film. Once 0 V was reached, constant-current discharges with different current densities and deposition time were applied to deposit Li. Cells for the morphology observation were disassembled after deposition. Cells for the cycling test were then stripped to 1 V.

For the full cell, cycling tests were carried out using battery testers (LANHE CT2001A). The batteries were tested in the voltage range of 2.8–4.4 V under a constant current, constant-voltage charge and a constant-current discharge mode. When the charge voltage reached the set cut-off, the constant-voltage charge process was applied until the charge current decayed to 0.05 C. The capacity retention was calculated on the third cycle capacity, after two formation cycles.

SEM

To perform morphological observation, cells were disassembled in an argon-filled glovebox. The deposited Li was washed with dimethyl carbonate to remove residual electrolytes. The morphology and thickness of the deposited Li were characterized using scanning electron microscopy (FEI Quanta 250 SEM). The cryogenic focused-ion beam milling was conducted using FEI Scios DualBeam FIB/SEM.

Cryo-TEM experiments

The samples used for TEM observations were prepared by the method illustrated in Supplementary Fig. 26. Specifically, FeF_3 was evaporated on a thin carbon film-supported Cu grid, which was assembled into a coin cell. After electrochemically converting FeF_3 into Fe/LiF nanocomposite, 0.1 mAh cm^{-2} Li was plated on it. The SEM image of the Li-deposited TEM grid was shown in Supplementary Fig. 27, where hexagonal-shaped Li crystals were observed, showing great agreement with Li plated on the Fe/LiF nanocomposite-modified Cu.

The cryo-TEM experiments were conducted in an FEI Talos F200X transmission electron microscope (operated at 200 kV) with an extreme Schottky field emission source and the four-quadrant EDS detectors. To keep the sample at cryogenic temperature (-−185 °C) in TEM, a Gatan liquid nitrogen holder with an anti-frost window was used to transfer the TEM sample at liquid nitrogen temperature. To prepare the TEM samples for the cryo-TEM experiments, we assembled coin cells with copper grids inserted onto a Cu foil electrode in a glovebox protected by an argon atmosphere. After electrochemical deposition, coin cells were disassembled, and the copper grids were sealed in aluminium pouch bags. The sealed grids were plunged into a liquid nitrogen bath and quickly loaded onto the pre-cooled cryo holder. With the protection of the anti-frost widow, the cryo holder was soon inserted into the TEM for further characterization. To perform the cryo-TEM tomography experiments, annular dark-field scanning transmission electron microscopy imaging mode was used to acquire tilt series with a maximum tilt range of ± 80°. The data were aligned by cross-correlation function and reconstructed by the simultaneous iterative reconstruction technique (SIRT) algorithm. The 3D tomographic reconstruction was visualized by Avizo.

XPS

XPS (Physical Electronics, Quantera Scanning XPS Microprobe System) was carried out using Al-anode source at 15 kV. Obtained data were calibrated based on the reference of C–C bond at 284.6 eV and fitted in CasaXPS. For FeF_3 XPS spectra, the noticeable C and O signals in the presented XPS results are probably a result of residual contaminants presents from air exposure during sample transfer into the XPS instrument.

Calculation of projected cell energy density

$$E_M = \frac{U_{avg} \times Q_{cell}}{(Q_{NMC}/Q_m^{NMC})/0.9 + Q_{Li}/Q_m^{Li} + m_{ele} \times Q_{cell} + m_{sep} + m_{cc}/2.0} \quad (1)$$

where E_M is the projected cell-level energy density; U_{avg} is the average cell operating voltage (3.8 V); Q_{cell} is the total areal capacity of the cell ($Q_{cell} = Q_{NMC} = 3.25$ mAh cm^{-2}, $Q_{Li} = 3.0$ mAh cm^{-2}, given N/P ratio is 0.92); Q_m^{NMC} is the specific capacity of NMC811 (200 mAh g^{-1}); cathode composition is $m_{NMC} : m_{PVDF} : m_{carbon} = 90:5:5$; Q_m^{Li} is the specific capacity of lithium (3,861 mAh g^{-1}); m_{ele} is the mass of electrolyte (3 g Ah^{-1}); m_{sep} is the areal mass of separator (0.0007 g cm^2); m_{cc} is the areal mass of current collector (0.00796 g cm^2 for Cu and 0.00324 g cm^2 for Al, double-sided electrode).

Data availability

All relevant data are included in the paper and its Supplementary Information. Source data are provided with this paper.

References

1. Kim, M. S. et al. Suspension electrolyte with modified Li^+ solvation environment for lithium-metal batteries. *Nat. Mater.* **21**, 445–454 (2022).
2. Yu, Z. et al. Rational solvent molecule tuning for high-performance lithium-metal battery electrolytes. *Nat. Energy* **7**, 94–106 (2022).
3. Liu, Y. et al. Self-assembled monolayers direct a LiF-rich interphase toward long-life lithium-metal batteries. *Science* **375**, 739–745 (2022).
4. Holoubek, J. et al. Electrolyte design implications of ion-pairing in low-temperature Li-metal batteries. *Energy Environ. Sci.* **15**, 1647–1658 (2022).
5. Xue, W. et al. Ultra-high-voltage Ni-rich layered cathodes in practical Li-metal batteries enabled by a sulfonamide-based electrolyte. *Nat. Energy* **6**, 495–505 (2021).
6. Niu, C. et al. Balancing interfacial reactions to achieve long cycle life in high-energy lithium-metal batteries. *Nat. Energy* **6**, 723–732 (2021).
7. Liu, H. et al. Ultrahigh Coulombic efficiency electrolyte enables Li||SPAN batteries with superior cycling performance. *Mater. Today* **42**, 17–28 (2021).
8. Holoubek, J. et al. Tailoring electrolyte solvation for Li-metal batteries cycled at ultra-low temperature. *Nat. Energy* **6**, 303–313 (2021).
9. Liu, H. et al. An anode-free Li-metal cell with replenishable Li designed for long cycle life. *Energy Storage Mater.* **36**, 251–256 (2021).
10. Hu, A. et al. An artificial hybrid interphase for an ultrahigh-rate and practical lithium-metal anode. *Energy Environ. Sci.* **14**, 4115–4124 (2021).
11. Yu, Z. et al. Molecular design for electrolyte solvents enabling energy-dense and long-cycling lithium-metal batteries. *Nat. Energy* **5**, 526–533 (2020).
12. Louli, A. J. et al. Diagnosing and correcting anode-free cell failure via electrolyte and morphological analysis. *Nat. Energy* **5**, 693–702 (2020).
13. Zhou, H., Yu, S., Liu, H. & Liu, P. Protective coatings for lithium-metal anodes: recent progress and future perspectives. *J. Power Sources* **450**, 227632 (2020).
14. Gao, Y. et al. Low-temperature and high-rate-charging lithium-metal batteries enabled by an electrochemically active monolayer-regulated interface. *Nat. Energy* **5**, 534–542 (2020).
15. Weber, R. et al. Long cycle life and dendrite-free lithium morphology in anode-free lithium pouch cells enabled by a dual-salt liquid electrolyte. *Nat. Energy* **4**, 683–689 (2019).
16. Niu, C. et al. High-energy lithium-metal pouch cells with limited anode swelling and long stable cycles. *Nat. Energy* **4**, 551–559 (2019).
17. Xiang, Y. et al. Quantitatively analyzing the failure processes of rechargeable Li-metal batteries. *Sci. Adv.* **7**, abj3423 (2021).

18. Hobold, G. M. et al. Moving beyond 99.9% Coulombic efficiency for lithium anodes in liquid electrolytes. *Nat. Energy* **6**, 951–960 (2021).
19. Zhao, Q. et al. On the crystallography and reversibility of lithium electrodeposits at ultrahigh capacity. *Nat. Commun.* **12**, 6034 (2021).
20. Chen, X., Zhao, B., Yan, C. & Zhang, Q. Review on Li deposition in working batteries: from nucleation to early growth. *Adv. Mater.* **33**, 2004128 (2021).
21. Zhang, Y. et al. Towards better Li-metal anodes: challenges and strategies. *Mater. Today* **33**, 56–74 (2020).
22. Zheng, J. et al. Regulating electrodeposition morphology of lithium: towards commercially relevant secondary Li-metal batteries. *Chem. Soc. Rev.* **49**, 2701–2750 (2020).
23. Fang, C., Wang, X. & Meng, Y. S. Key issues hindering a practical lithium-metal anode. *Trends Chem.* **1**, 152–158 (2019).
24. Fang, C. et al. Quantifying inactive lithium in lithium-metal batteries. *Nature* **572**, 511–515 (2019).
25. Lv, D. et al. Failure mechanism for fast-charged lithium-metal batteries with liquid electrolytes. *Adv. Energy Mater.* **5**, 1400993 (2015).
26. Wu, Z. et al. The role of ion transport in the failure of high-areal-capacity Li-metal batteries. *ACS Energy Lett.* **7**, 2701–2710 (2022).
27. Zhang, J. G., Xu, W., Xiao, J., Cao, X. & Liu, J. Lithium-metal anodes with nonaqueous electrolytes. *Chem. Rev.* **120**, 13312–13348 (2020).
28. Ren, X. et al. Enabling high-voltage lithium-metal batteries under practical conditions. *Joule* **3**, 1662–1676 (2019).
29. Fang, C. et al. Pressure-tailored lithium deposition and dissolution in lithium-metal batteries. *Nat. Energy* **6**, 987–994 (2021).
30. Chen, T. et al. Ultra-low concentration electrolyte enabling LiF-rich SEI and dense plating/stripping processes for lithium-metal batteries. *Adv. Sci.* **9**, 2203216 (2022).
31. Sun, H. H. et al. In situ formation of a multicomponent inorganic-rich SEI layer provides a fast-charging and high-specific-energy Li-metal battery. *J. Mater. Chem. A* **7**, 17782–17789 (2019).
32. Fan, X. et al. Non-flammable electrolyte enables Li-metal batteries with aggressive cathode chemistries. *Nat. Nanotechnol.* **13**, 715–722 (2018).
33. Liu, J. et al. Pathways for practical high-energy long-cycling lithium-metal batteries. *Nat. Energy* **4**, 180–186 (2019).
34. Sun, J. et al. Li deposition mechanism on Si and Cu substrates in the carbonate electrolyte. *Energy Environ. Sci.* https://doi.org/10.1039/d2ee01833k (2022).
35. Cui, S. et al. Large-scale modification of commercial copper foil with lithiophilic metal layer for Li-metal battery. *Small* **16**, 1905620 (2020).
36. Lin, D., Liu, Y. & Cui, Y. Reviving the lithium-metal anode for high-energy batteries. *Nat. Nanotechnol.* **12**, 194–206 (2017).
37. Yan, K. et al. Selective deposition and stable encapsulation of lithium through heterogeneous seeded growth. *Nat. Energy* **1**, 16010 (2016).
38. Lee, D. et al. Copper nitride nanowires printed Li with stable cycling for Li-metal batteries in carbonate electrolytes. *Adv. Mater.* **32**, 1905573 (2020).
39. Niu, C. et al. Self-smoothing anode for achieving high-energy lithium-metal batteries under realistic conditions. *Nat. Nanotechnol.* **14**, 594–601 (2019).
40. Li, Z. et al. Gradient nano-recipes to guide lithium deposition in a tunable reservoir for anode-free batteries. *Energy Storage Mater.* **45**, 40–47 (2022).
41. Yang, C. et al. Ultrafine silver nanoparticles for seeded lithium deposition toward stable lithium-metal anode. *Adv. Mater.* **29**, 1702714 (2017).
42. Lu, Y. et al. Spatially controlled lithium deposition on silver-nanocrystals-decorated TiO_2 nanotube arrays enabling ultrastable lithium-metal anode. *Adv. Funct. Mater.* **31**, 2009605 (2021).
43. Hao, F., Verma, A. & Mukherjee, P. P. Mesoscale complexations in lithium electrodeposition. *ACS Appl. Mater. Interfaces* **10**, 26320–26327 (2018).
44. Coaty, C., Zhou, H., Liu, H. & Liu, P. A scalable synthesis pathway to nanoporous metal structures. *ACS Nano* **12**, 432–440 (2018).
45. Zhang, X.-Q. et al. Columnar lithium-metal anodes. *Angew. Chem. Int. Ed.* **56**, 14207–14211 (2017).
46. Qian, J. et al. Dendrite-free Li deposition using trace-amounts of water as an electrolyte additive. *Nano Energy* **15**, 135–144 (2015).
47. Saifullah, M. S. M., Botton, G. A., Boothroyd, C. B. & Humphreys, C. J. Electron energy loss spectroscopy studies of the amorphous to crystalline transition in FeF_3. *J. Appl. Phys.* **86**, 2499–2504 (1999).
48. Li, T., Li, L., Cao, Y. L., Ai, X. P. & Yang, H. X. Reversible three-electron redox behaviors of FeF_3 nanocrystals as high-capacity cathode-active materials for Li-ion batteries. *J. Phys. Chem. C* **114**, 3190–3195 (2010).
49. Wang, J. et al. Fundamental study on the wetting property of liquid lithium. *Energy Storage Mater.* **14**, 345–350 (2018).
50. Shi, L., Bak, S., Shadike, Z. & Wang, C. Reaction heterogeneity in practical high-energy lithium–sulfur pouch cells. *Energy Environ. Sci.* **13**, 3620–3632 (2020).
51. Li, Y. et al. Atomic structure of sensitive battery materials and interfaces revealed by cryo–electron microscopy. *Science* **358**, 506–510 (2017).
52. Yamakawa, N., Jiang, M., Key, B. & Grey, C. P. Identifying the local structures formed during lithiation of the conversion material, iron fluoride, in a Li ion battery: a solid-state NMR, X-ray diffraction, and pair distribution function analysis study. *J. Am. Chem. Soc.* **131**, 10525–10536 (2009).
53. Zheng, H. et al. Grain boundary properties of elemental metals. *Acta Mater.* **186**, 40–49 (2020).
54. Tran, R. et al. Surface energies of elemental crystals. *Sci. Data* **3**, 160080 (2016).
55. Tran, R. et al. Anisotropic work function of elemental crystals. *Surf. Sci.* **687**, 48–55 (2019).
56. Shi, F. et al. Strong texturing of lithium-metal in batteries. *Proc. Natl Acad. Sci. USA* **114**, 12138–12143 (2017).
57. Adams, B. D., Zheng, J., Ren, X., Xu, W. & Zhang, J. Accurate determination of Coulombic efficiency for lithium-metal anodes and lithium-metal batteries. *Adv. Energy Mater.* **8**, 1702097 (2018).
58. Li, Q. et al. Homogeneous interface conductivity for lithium dendrite-free anode. *ACS Energy Lett.* **3**, 2259–2266 (2018).
59. Heim, F., Kreher, T. & Birke, K. P. The influence of micro-structured anode current collectors in combination with highly concentrated electrolyte on the Coulombic efficiency of in situ deposited Li-metal electrodes with different counter electrodes. *Batteries* **6**, 20–30 (2020).
60. Wang, J. et al. Improving cyclability of Li-metal batteries at elevated temperatures and its origin revealed by cryo-electron microscopy. *Nat. Energy* **4**, 664–670 (2019).
61. Biswal, P. et al. The early-stage growth and reversibility of Li electrodeposition in Br-rich electrolytes. *Proc. Natl Acad. Sci. USA* **118**, e2012071118 (2021).
62. Chen, S. et al. Critical parameters for evaluating coin cells and pouch cells of rechargeable Li-metal batteries critical parameters for evaluating coin cells and pouch cells of rechargeable Li-metal batteries. *Joule* **3**, 1094–1105 (2019).
63. Kim, M. S. et al. Langmuir–Blodgett artificial solid-electrolyte interphases for practical lithium-metal batteries. *Nat. Energy* **3**, 889–898 (2018).
64. Chen, H. et al. Tortuosity effects in lithium-metal host anodes. *Joule* **4**, 938–952 (2020).

Acknowledgements
The work was supported by the Office of Vehicle Technologies of the US Department of Energy through the Advanced Battery Materials Research Program (Battery500 Consortium) under contract no. DE-EE0007764. Work done by C.W. and H.L.X. at UCI was supported by the Materials Science and Engineering Divisions, Office of Basic Energy Sciences of the US Department of Energy, under award no. DE-SC0021204. Part of the work used the UCSD-MTI Battery Fabrication Facility and the UCSD-Arbin Battery Testing Facility. Part of the characterization was performed at the San Diego Nanotechnology Infrastructure of UCSD, a member of the National Nanotechnology Coordinated Infrastructure, which is supported by the National Science Foundation (grant ECCS-1542148). This research used the TEM facility of the Center for Functional Nanomaterials, which is a US Department of Energy Office of Science User Facility, at Brookhaven National Laboratory under contract no. DE-SC0012704.

Author contributions
Z.W. and P.L. conceived the idea. P.L. and H.L. directed the project. Z.W. and Z.H. performed the electrochemical experiments and SEM characterizations. S.W. performed the FIB-SEM analysis. S.Y. carried out the XPS characterization. X.X. developed the method for the thermal evaporation of iron fluoride. J.H. provided input on data interpretation and manuscript preparation. Q.M. helped with the contact angle measurement. C.W. and H.L.X. performed the TEM measurement and analysis. Z.W., C.W., Z.H., H.L., J.H., H.L.X. and P.L. co-wrote and revised the manuscript.

Competing interests
The authors declare no competing interests.

Additional information
Supplementary information The online version contains supplementary material available at https://doi.org/10.1038/s41560-023-01202-1.

Correspondence and requests for materials should be addressed to Huolin L. Xin or Ping Liu.

Peer review information *Nature Energy* thanks Maximilian Becker and the other, anonymous, reviewer(s) for their contribution to the peer review of this work.